



# Refining Space Object Radiation Pressure Modeling with Bidirectional Reflectance Distribution Functions

Charles J. Wetterer\*

*Pacific Defense Solutions, Kihei, Hawaii 96753*

Richard Linares<sup>†</sup> and John L. Crassidis<sup>‡</sup>

*University at Buffalo, State University of New York, Amherst, New York 14260*

Thomas M. Kelecy<sup>§</sup>

*Boeing LTS, Colorado Springs, Colorado 80919*

Marek K. Ziebart<sup>¶</sup>

*University College London, London, England WC1E 6BT, United Kingdom*

Moriba K. Jah<sup>\*\*</sup>

*U.S. Air Force Research Laboratory, Space Vehicles Directorate, Kirtland Air Force Base, New Mexico 87117*

and

Paul J. Cefola<sup>††</sup>

*University at Buffalo, State University of New York, Amherst, New York 14260*

DOI: 10.2514/1.60577

High-fidelity orbit propagation requires detailed knowledge of the solar radiation pressure on a space object. The solar radiation pressure depends not only on the space object's shape and attitude, but also on the absorption and reflectance properties of each surface on the object. These properties are typically modeled in a simplistic fashion, but are here described by a surface bidirectional reflectance distribution function. Several analytic bidirectional reflectance distribution function models exist, and are typically complicated functions of illumination angle and material properties represented by parameters within the model. In general, the resulting calculation of the solar radiation pressure would require a time-consuming numerical integration. This might be impractical if multiple solar radiation pressure calculations are required for a variety of material properties in real time; for example, in a filter where the particular surface parameters are being estimated. This paper develops a method to make accurate and precise solar radiation pressure calculations quickly for some commonly used analytic bidirectional reflectance distribution functions. In addition, other radiation pressures exist, including Earth albedo/Earth infrared radiation pressure, and thermal radiation pressure from the space object itself, and are influenced by the specific bidirectional reflectance distribution function. A description of these various radiation pressures and a comparison of the magnitude of the resulting accelerations at various orbital heights and the degree to which they affect the space object's orbit are also presented. Significantly, this study suggests that, for space debris whose interactions with electro-magnetic radiation are described accurately with a bidirectional reflectance distribution function, then hitherto unmodeled torques would account for rotational characteristics affecting both tracking signatures and the ability to predict the orbital evolution of the objects.

## I. Introduction

Received 3 October 2012; accepted for publication 5 April 2013; published online 18 October 2013. Copyright © 2013 by the American Institute of Aeronautics and Astronautics, Inc. The U.S. Government has a royalty-free license to exercise all rights under the copyright claimed herein for Governmental purposes. All other rights are reserved by the copyright owner. Copies of this paper may be made for personal or internal use, on condition that the copier pay the \$10.00 per-copy fee to the Copyright Clearance Center, Inc., 222 Rosewood Drive, Danvers, MA 01923; include the code 1533-3884/13 and \$10.00 in correspondence with the CCC.

\*Principal Scientist, 1300 N. Holopono St. Suite 116; jack.wetterer@pacificds.com.

<sup>†</sup>Graduate Student, Department of Mechanical and Aerospace Engineering; linares2@buffalo.edu. Student Member AIAA.

<sup>‡</sup>CUBRC Professor in Space Situational Awareness, Department of Mechanical and Aerospace Engineering; johnc@buffalo.edu. Associate Fellow AIAA.

<sup>§</sup>Senior Scientist, 5555 Tech Center Dr., Suite 400; Thomas.M.Kelecy@boeing.com.

<sup>¶</sup>Professor of Space Geodesy, Department of Civil, Environmental and Geomatic Engineering; m ziebart@ucl.ac.uk.

<sup>\*\*</sup>Senior Aerospace Engineer; Associate Fellow AIAA.

<sup>††</sup>Adjunct Professor, Department of Mechanical and Aerospace Engineering; also Consultant in Aerospace Systems, Spaceflight Mechanics, and Astrodynamics; paulcefo@buffalo.edu. Associate Fellow AIAA.

**O**BSERVATIONS made on uncontrolled high area-to-mass ratio (HAMR) debris objects in near geosynchronous orbit (GEO) indicate they can have apparent effective area-to-mass ratio (AMR) values ranging anywhere from 0.1 to tens of meters squared per kilogram [1]. Only a subset of these observations produced this result out of many more detections that remain unassociated to unique objects. In other words, there is an as-of-yet unquantified population of space objects (SOs) near the GEO region due to an inability in converting optical detections into predictable orbits that allow proper data association. Because the detections obtained for any specific object are sparse, the modeling of the dynamic behavior of the SO is critical for successful object reacquisition and data association. Previous analyses have shown that HAMR objects have AMR values that vary with time and produce significant variations over relatively short periods of time (days to weeks) [2,3]. This is likely due to stochastic solar radiation pressure (SRP) accelerations resulting from time varying solar illumination due to orientation changes with respect to the sun and solar eclipsing periods. These in turn result in time varying reflective and emissive accelerations that are difficult to predict. This intuitively makes sense given that these objects are uncontrolled and their motion is driven by their interaction with a dynamic space environment (i.e., processes that are both deterministic and stochastic). Reference [4] presents a detailed SRP

formulation that models the time varying orientation and surface thermal characteristics of HAMR objects in space, and quantifies the perturbation errors due to a variety of modeling assumptions in the determination and prediction of the orbits of these objects. It is shown that the errors due to the mismodeling of thermal emissions are large enough to result in significant errors in the orbit predictions and, in particular, can result in unbalanced accelerations in directions orthogonal to the object–sun line. The analysis examined the sensitivity to the lack of a priori knowledge of attitude, shape, or materials. The perturbations resulting from unmodeled dynamics due to inadequate shape/attitude knowledge and radiation pressure models explain, at least partly, the discrepancies between the vast literature on theoretical long-term orbital histories, actual observed behavior for a subset of optical detections that have been successfully correlated to unique objects, and the lack of success in adjudicating the remainder of optical detections.

The physical correlation between the SO's shape/attitude and its orbital position due to the various nongravitational forces and torques, such as the SRP, which depend on shape and attitude, can be used to determine physical characteristics about the object. For example, with angles data alone, it is possible to infer an effective albedo area to mass ratio as shown in [5,6]. The observability of this parameter is due to the SRP perturbation effects experienced by the SO indirectly observed in the line-of-sight data. The surface reflectance parameters, such as albedo, influencing the SO's dynamics are the same surface reflectance parameters that determine the object's observed brightness. This is the physical link that enables both angles (astrometric line-of-sight) and brightness (photometric flux intensity) measurements to be fused and exploited for the purpose of simultaneous orbit, attitude, and shape determination of an SO. It is theoretically demonstrated that simultaneously processing both astrometric and photometric measurements enables shape and attitude estimates that leads to improved orbit propagation [7].

High-fidelity orbit propagation is necessary to reacquire a HAMR object over significant temporal sparseness in observations. For this process to yield accurate results, however, the model used to calculate the brightness of the SO must be physically consistent with the model used to calculate the SRP and other nongravitational forces and torques. Brightness models are based on the surface bidirectional reflectance distribution function (BRDF), where BRDFs define how the diffuse and specular components of light are reflected from the surface. However, SRP calculations typically use an idealized BRDF in developing the characteristic equation and, in some cases, a simplified shape model (e.g., a diffuse cannonball). In this paper, the SRP calculation is reconciled with more physically realistic BRDF functions.

The work presented here aims to show the importance of properly accounting for the BRDF when considering radiation pressure accelerations. First, the dependence of the SRP on the BRDF is demonstrated in Sec. II and descriptions of two commonly used BRDFs are presented in Sec. III. The correction factors required in the procedure used to reconcile the SRP to the BRDF are then calculated in Sec. IV. Other radiation pressures, the Earth–albedo/Earth–infrared radiation pressure (ERP), and the thermal radiation pressure (TRP) are described in Sec. V along with how these are reconciled with the BRDF. For the TRP, this requires the development of a completely new model. Finally, the deterministic orbit and attitude propagation equations used in the analysis are described in Sec. VI and a comparison of the magnitude of the various radiation pressures and the resulting propagation errors on a HAMR object is presented in Sec. VII.

## II. SRP Dependence on BRDF

The BRDF ( $f_r$ ) defines how light is reflected from an opaque surface with a given surface normal direction  $\hat{N}$ , illumination direction  $\hat{L}$  with  $\theta_i$  the normal angle from  $\hat{N}$  and  $\phi_i$  the azimuth from the  $x$  axis, and observer direction  $\hat{V}$  with  $\theta_r$  the normal angle from  $\hat{N}$  and  $\phi_r$  the azimuth from the  $x$  axis, as shown in Fig. 1, and is given by

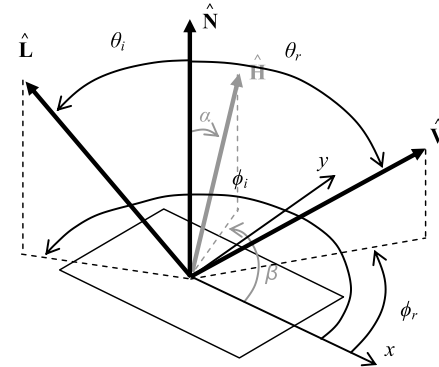


**Fig. 1** The geometry of reflection.

$$f_r(\theta_i, \phi_i; \theta_r, \phi_r; \lambda) = \frac{dL_r(\theta_r, \phi_r; \lambda)}{dE_i(\theta_i, \phi_i; \lambda)} \quad (1)$$

where  $dL_r$  is the reflected radiance in  $\text{W} \cdot \text{m}^{-2} \text{sr}^{-1}$ ,  $dE_i$  is the irradiance in  $\text{W} \cdot \text{m}^{-2}$ , and  $\lambda$  is the wavelength. The bisector vector between the illumination source and the observer is  $\hat{H} = (\hat{L} + \hat{V})/|\hat{L} + \hat{V}|$  with  $\alpha$  the normal angle from  $\hat{N}$  and  $\beta$  the azimuth from the  $x$  axis. These are also shown in Fig. 1 and are used later in the BRDF models.

The acceleration caused by the SRP can be calculated by summing the individual contributions of all the constituent illuminated “facets” that make up the object, where a facet is defined as a flat surface of a particular area and surface normal direction. The acceleration is

$$\mathbf{a}_{\text{SRP}} = - \sum_{k=1}^{N_{\text{facets}}} \int_0^\infty \frac{F_i(\lambda) A_k f_k(\hat{L} \cdot \hat{N}_k)_+}{m_{\text{so}} c} \times \left[ \hat{L} + \left( \int_0^{2\pi} \int_0^{\pi/2} f_r \cos \theta_r \hat{V} d\theta_r d\phi_r \right)_k \right] d\lambda \quad (2)$$

where  $F_i(\lambda)$  is the solar flux (in  $\text{W} \cdot \text{m}^{-2} \text{nm}^{-1}$ ),  $A_k$  is the facet area,  $f_k$  is the fraction of the facet that is illuminated (due to self-shadowing),  $m_{\text{so}}$  is the mass of the object,  $c$  is the speed of light,  $N_{\text{facets}}$  is the total number of facets, and the BRDF for each facet is integrated over all observer directions and all wavelengths. In addition,  $(x)_+ = xH(x)$  where  $H(x)$  is the Heaviside step function, which is unity for positive values and zero elsewhere. The first term in parentheses in Eq. (2) is simply the acceleration resulting from the momentum exchange of the incoming photons, and the second term in parentheses is the acceleration resulting from the fraction of incoming photons reflected by the surface.

In an effort to establish a common nomenclature, the general BRDF is calculated using

$$f_r = (dR_d + sR_s) \quad (3)$$

which depends on the diffuse bidirectional reflectance  $R_d$  and the specular bidirectional reflectance  $R_s$  and the fraction of each to the total reflectance ( $d$  and  $s$ , respectively, where  $d + s = 1$ ), which again is in and of itself a fraction of the total incoming energy.

In general,  $R_d$  and  $R_s$  are complicated functions of illumination angle and material properties represented by parameters within the particular BRDF model. For certain BRDFs, however, the integral can be solved analytically. For example, the BRDF with a Lambertian diffuse component and purely “mirror-like” specular component (where  $\hat{R} = 2(\hat{L} \cdot \hat{N})\hat{N} - \hat{L}$  is the direction of mirror-like reflection of  $\hat{L}$ ) is given by

$$f_r = d\left(\frac{\rho}{\pi}\right) + s\left[\frac{F_0 \delta(\hat{V} - \hat{R})}{\cos \theta_i}\right] \quad (4)$$

where  $\rho$  is the diffuse reflectance ( $0 \leq \rho \leq 1$ ),  $F_0$  is the specular reflectance of the surface at normal incidence ( $0 \leq F_0 \leq 1$ ), and  $\delta$  is the delta function, which yields an acceleration due to the SRP of



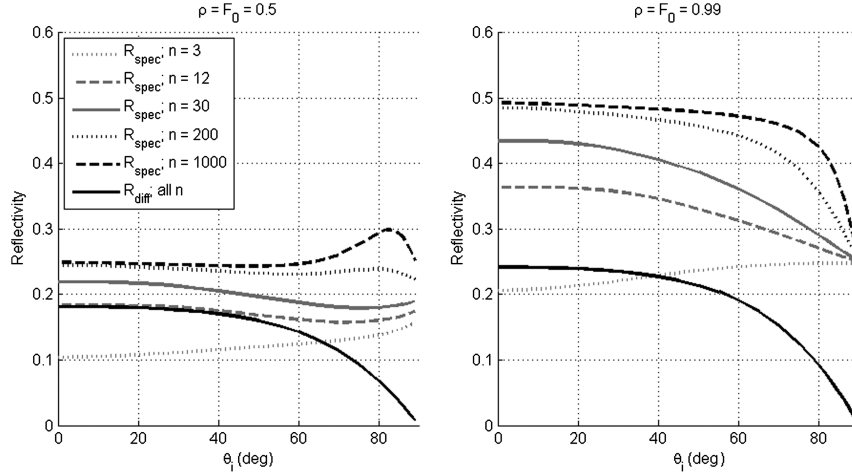


Fig. 2 Ashikhmin–Shirley diffuse and specular reflectivity.

$$n_{\text{est}} = \frac{1 + \sqrt{F_0}}{1 - \sqrt{F_0}}$$

In addition to  $d$ ,  $\rho$ , and  $F_0$ , the Cook–Torrance BRDF has a facet slope  $m$  parameter that defines the reflectance properties of each surface. The facet slope parameter of the Cook–Torrance BRDF and the exponential factor of the Ashikhmin–Shirley BRDF are roughly related by  $n = 2/m^2$ .

Figure 3 shows the dependence of  $R_{\text{diff}}$  and  $R_{\text{spec}}$  on illumination angle and exponential factor for the Cook–Torrance BRDF where the integrals of Eqs. (7) and (8) are computed numerically and  $d = s = 0.5$ . Again, the simple BRDF of Eq. (4) yields  $R_{\text{diff}} = R_{\text{spec}} = 0.25$  and 0.495 for the left and right plots, respectively, and so the deviations of the Cook–Torrance BRDF model from the simple BRDF are smaller. Specifically, the Lambertian diffuse portion is the same and produces a constant diffuse reflectivity. The specular portion becomes more mirror-like for smaller values of facet slope, although with differences in the reflectivity at high solar illumination angles. In all cases, energy is conserved.

In general, the parameters that comprise a BRDF model are wavelength dependent. For simplicity, this wavelength dependence is ignored and SRP correction factors for constant parameter values are derived. Accounting for the wavelength dependence would simply involve a sum of separate solutions weighted by the solar flux at that particular wavelength.

#### IV. Deriving the SRP Delta Factors

The diffuse component of the Cook–Torrance BRDF is Lambertian and, thus, the diffuse  $\Delta$  factor is simply unity. The diffuse

component of the Ashikhmin–Shirley BRDF is non-Lambertian, but the integral of Eq. (2) can be evaluated analytically. The resulting diffuse  $\Delta$  factors are

$$\Delta_{d-\text{AS}}(\theta_i, sF_0) = \left[ \frac{31}{32} (1 - sF_0) \right] \left( \frac{1573}{1426} \right) \left[ 1 - \left( 1 - \frac{\cos \theta_i}{2} \right)^5 \right] \quad (19)$$

$$\Delta_{d-\text{CT}} = 1 \quad (20)$$

where the product of  $\rho$  and the term in the first square brackets in Eq. (19) is the equivalent Lambertian diffuse reflectance for the Ashikhmin–Shirley BRDF.

Values for the specular  $\Delta$  factors can be numerically calculated at a particular illumination angle and set of BRDF parameters by comparing the numerical integration of the BRDF in Eq. (2),

$$\mathbf{L}' = \int_0^{2\pi} \int_0^{\pi/2} f_r(\hat{\mathbf{V}} \cdot \hat{\mathbf{N}}, \lambda) \cos \theta_r \hat{\mathbf{V}} d\theta_r d\phi_r \quad (21)$$

to the equivalent portion of Eq. (6) when only considering the specular component:

$$\mathbf{L}' = (1 - \Delta_{s1} F_0) \hat{\mathbf{L}} + (2 \Delta_{s2} F_0 \hat{\mathbf{L}} \cdot \hat{\mathbf{N}}) \hat{\mathbf{N}} \quad (22)$$

Specifically, for  $\hat{\mathbf{L}} \neq \hat{\mathbf{N}}$ ,

$$\Delta_{s1}(p, \theta_i)_{\text{numerical}} = \frac{(\mathbf{L}' \cdot \hat{\mathbf{N}}) \cos \theta_i - (\mathbf{L}' \cdot \hat{\mathbf{L}})}{F_0 \sin^2 \theta_i} \quad (23)$$

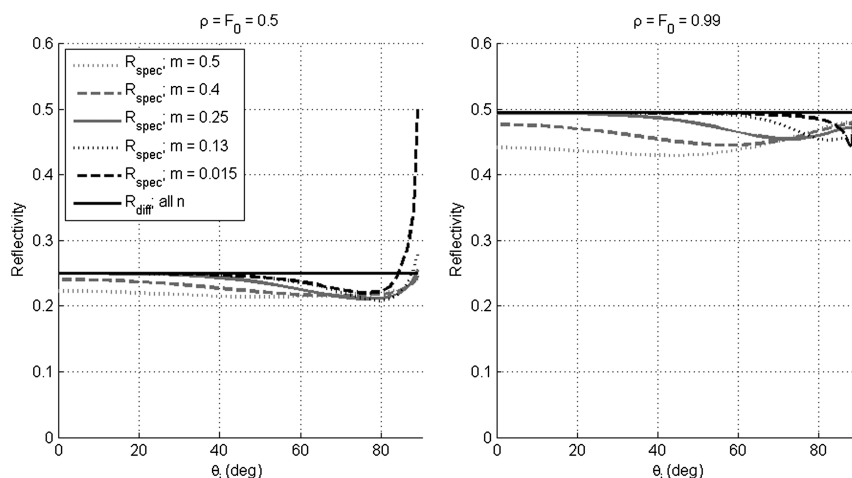
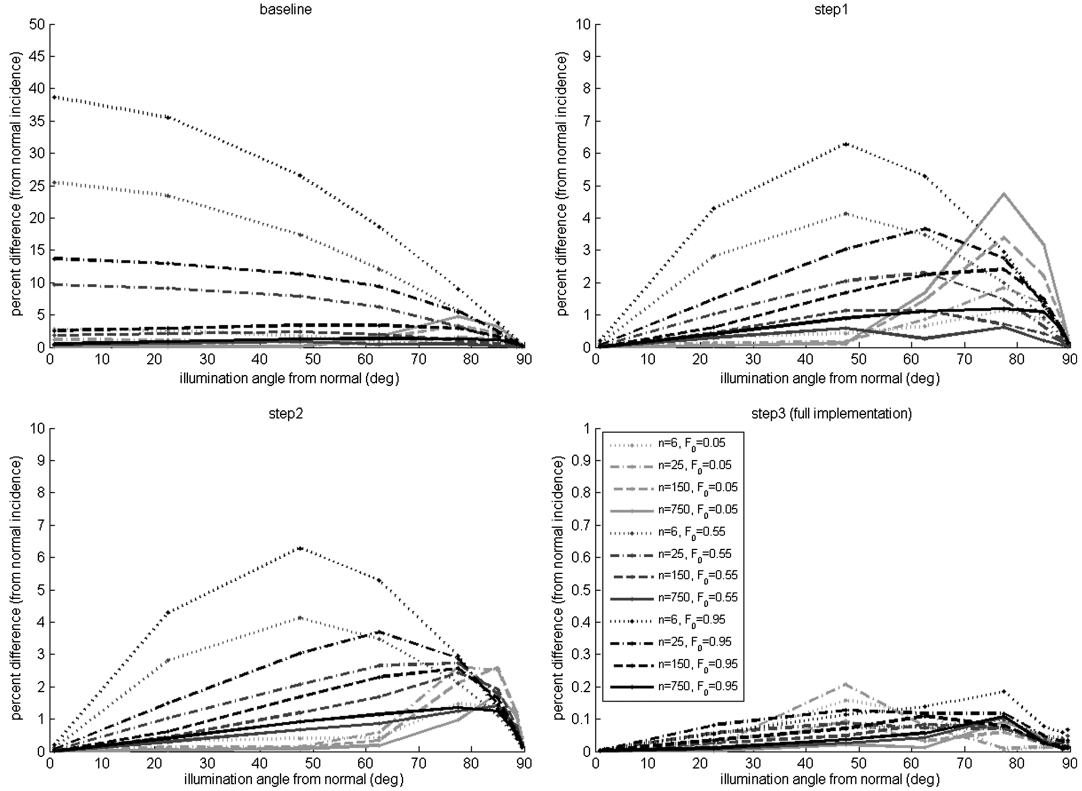


Fig. 3 Cook–Torrance diffuse and specular reflectivity.





**Fig. 4** Percentage difference (to acceleration at normal incidence) for Ashikhmin–Shirley BRDF.

## V. Other Radiation Pressure Models

Other sources of radiation pressure exist where the difference from the baseline of Eq. (5) are comparable to the BRDF SRP correction of Eq. (6). Earth–albedo and Earth–infrared radiation pressure (ERP) is identical in form to the SRP where Earth’s reflection in the visible and emission in the infrared takes the place of the sun as the illumination source. Calculation of the ERP acceleration is more complicated due

to the larger solid angle subtended by Earth with respect to the SO and the introduction of an empirical model to represent Earth’s albedo and emissivity. As with the SRP acceleration, the SO’s surface BRDF also needs to be considered. The final radiation pressure to be considered is the SO’s thermal radiation pressure (TRP). To calculate the TRP acceleration, the temperatures of the various surfaces of the SO must be known. This requires a model that calculates these temperatures

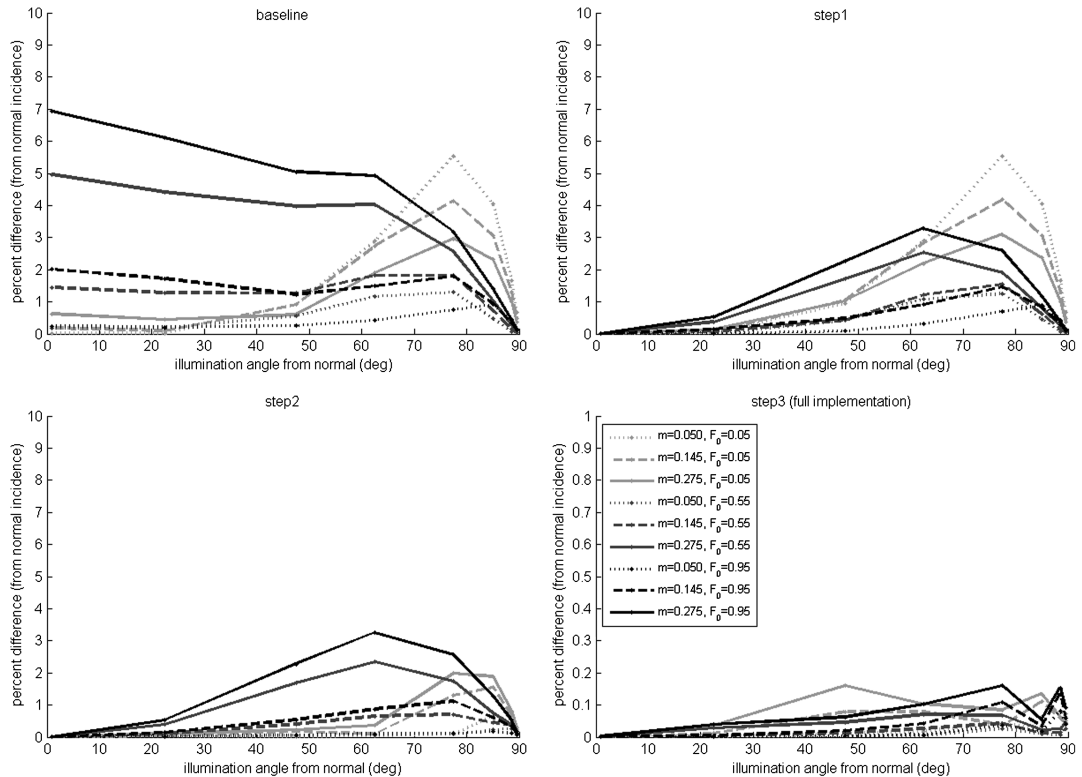


**Fig. 5** Percentage difference (to acceleration at normal incidence) for Cook–Torrance BRDF.







time. Each surface of the cube is identical with  $\rho = F_0 = 0.5$  and  $d = s = 0.5$ .

In this simulation, the initial attitude, using the quaternion parameterization, is set to  $\mathbf{q} = [0.7041; 0.0199; 0.0896; 0.7041]^T$ , the initial angular rate is zero, and the values are propagated for seven days with a 6 s time step. The initial date and time are 15 March 2010, 0400 hrs. It should be noted that these tests are designed to highlight the differing trajectory and attitude behaviors predicted by the various radiation pressures (SRP vs ERP vs TRP) and the two modeling approaches (traditional SRP vs BRDF-corrected SRP).

Figures 9 and 10 plot the absolute magnitude of the various radiation forces as a function of time for the HAMR object at GEO and LEO, respectively, for the last half-day of the simulation. Also plotted are the fractional differences of the BRDF-corrected SRP to the simplified SRP ( $|a_{\text{SRP-AS}} - a_{\text{SRP}}|/|a_{\text{SRP}}|$  and  $|a_{\text{SRP-CT}} - a_{\text{SRP}}|/|a_{\text{SRP}}|$ ) and the relative difference of the ERP and TRP to the simplified SRP ( $|a_{\text{ERP}}|/|a_{\text{SRP}}|$  and  $|a_{\text{TRP}}|/|a_{\text{SRP}}|$ ) for times when the object is out of eclipse. Whereas the relative magnitude of the TRP and difference of the BRDF-corrected SRP to the SRP remains about the same for each orbit type, the magnitude of the ERP depends on radial distance, as expected. Note the regular entry into and exit out of Earth eclipse in the acceleration time histories coincident with the orbit of the satellite.

Of particular note is the variation in magnitude of the BRDF-corrected SRPs to the others. This results from the fact that only the BRDF-corrected SRPs produce a torque on the HAMR object resulting in attitude changes and thus variations in the projected area and resulting acceleration. For a rectangular prism,  $r_k^B A(\mathbf{q})$  in Eq. (55) is proportional to  $\hat{\mathbf{N}}_k$  for each surface. When combined with the simplified SRP in Eq. (5) with all the surfaces having the same reflectance properties, this reduces to the torque being proportional to

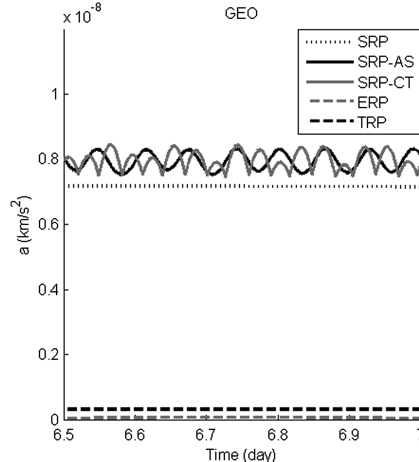


Fig. 9 Absolute magnitude of radiation force, and fractional difference for out of eclipse times for GEO.

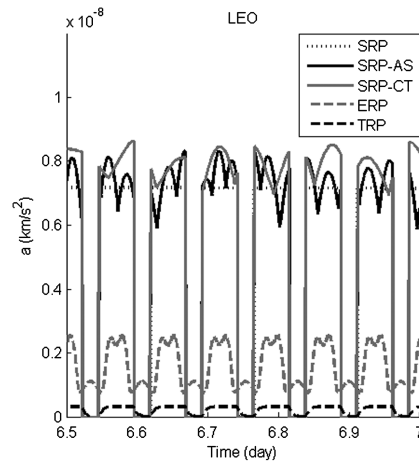


Fig. 10 Absolute magnitude of radiation force, and fractional difference for out of eclipse times for LEO.

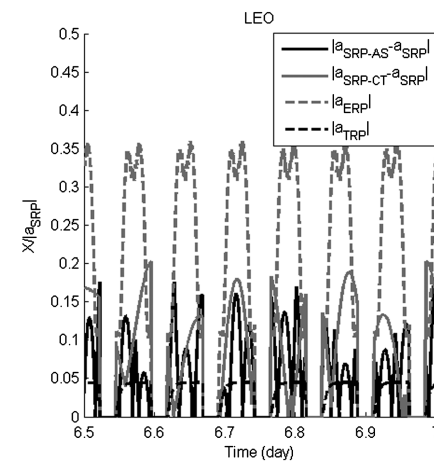
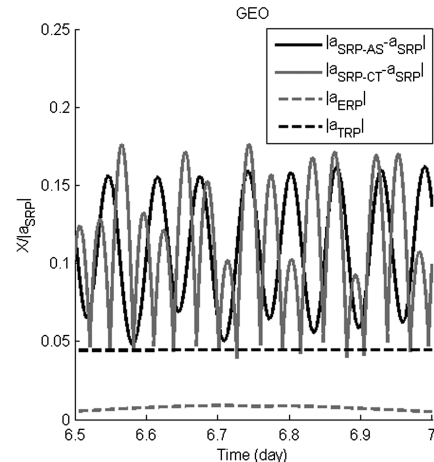
$$\mathbf{M} \propto \sum_{k=1}^{N_{\text{facets}}} (\hat{\mathbf{L}} \cdot \hat{\mathbf{N}}_k)_+ (\hat{\mathbf{L}} \times \hat{\mathbf{N}}_k) \quad (56)$$

Because the surface normals of adjacent sides of a rectangular prism are orthogonal, this summation is zero for any vector  $\hat{\mathbf{L}}$ . Thus, for the SRP and ERP (with the simple Lambertian diffuse and mirror-like specular BRDF), the torque is always zero. For the TRP, the acceleration due to each surface is along the surface normal per Eq. (39), and so, when combined with Eq. (55), is also always zero for a rectangular prism. When combining Eq. (55) with the BRDF-corrected SRP in Eq. (6), however, the torque is now proportional to

$$\mathbf{M} \propto \sum_{k=1}^{N_{\text{facets}}} [1 - sF_0(\Delta_{s1})_k] (\hat{\mathbf{L}} \cdot \hat{\mathbf{N}}_k)_+ (\hat{\mathbf{L}} \times \hat{\mathbf{N}}_k) \quad (57)$$

The introduction of the  $\Delta$  factor, which depends also on illumination angle and could be different for each surface, results in a net torque. This difference between the rotational dynamics of the SO when using the simplistic SRP of Eq. (5) and the BRDF-corrected SRP of Eq. (6), highlighted by the discovery of a hitherto unmodeled torque caused by the specular reflectance of the SO's surface, underscores the reason for this work as motivated in the introduction of this paper.

Figures 11 and 12 plot the total difference, radial difference, in-track difference, and cross-track difference for positions calculated using the BRDF-corrected SRP (both Ashikhmin–Shirley and Cook–Torrance), simplified SRP + ERP, and simplified SRP + TRP as compared to the position with simplified SRP only as a function of time for the last half-day of the simulation. In this particular simulation, the two BRDF-corrected SRPs show the largest variation



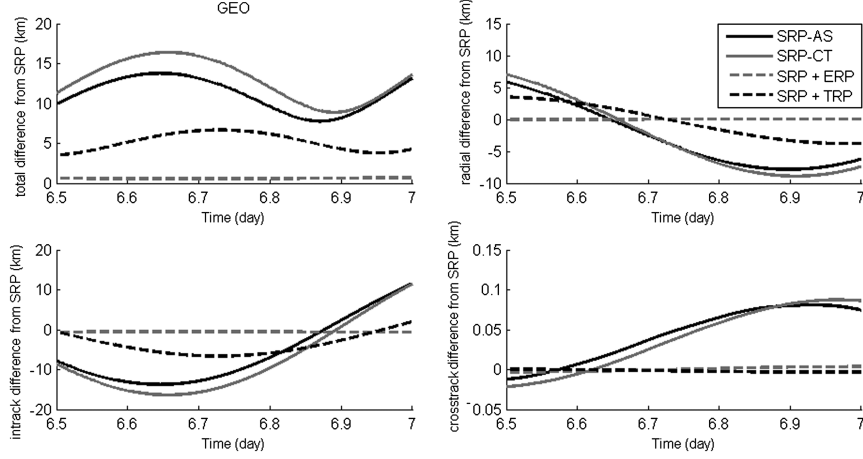


**Fig. 11** Total, radial, in-track, and cross-track differences in position from simplified SRP-only case for GEO.

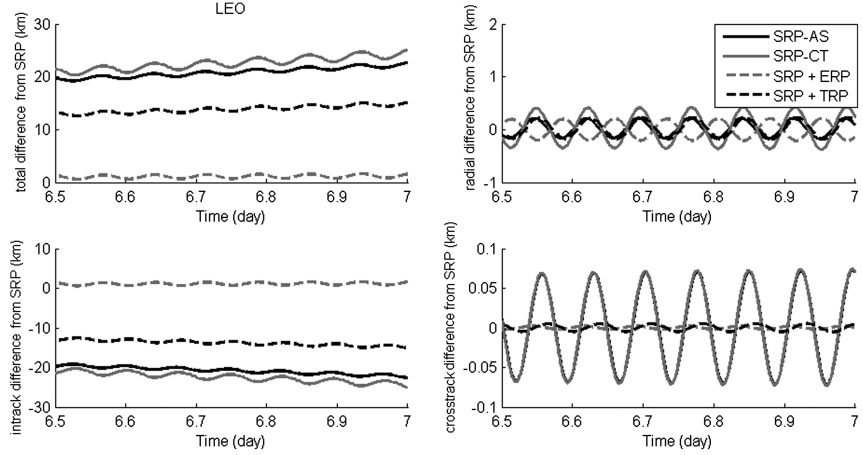


**Fig. 12** Total, radial, in-track, and cross-track differences in position from simplified SRP-only case for LEO.

followed by the TRP and then the ERP with only minor differences. Variations in orbit, SO shape, and surface properties would undoubtedly produce different magnitudes. For high-fidelity orbit propagation, all these nongravitational forces need to be accounted for. In addition, the fact that the BRDF-corrected SRPs are similar, although not identical, is encouraging but highlights the need for further research regarding which BRDF model is the closest representation of the true BRDF of SO surfaces.

### VIII. Conclusions

Brightness models are dependent on the surface bidirectional reflectance distribution function (BRDF). Current radiation pressure models, however, ignore the BRDF, even though the BRDF has a significant effect on the magnitude and direction of the resulting radiation pressures. The BRDF-induced perturbations in the solar radiation pressure (SRP) are significant enough to affect both tracking signatures and the ability to predict the orbital and attitudinal evolution of a space object (SO). The SRP, as well as the Earth-albedo/Earth-infrared radiation pressure and the thermal radiation pressure can be made physically consistent with the BRDF. For these results to be fully used, however, additional analyses regarding which analytic BRDF model best matches the true BRDF of the SO surfaces are needed.

### Appendix A:

In the step 1 derivations of Sec. IV with  $s = 1$  and  $\hat{L} = \hat{N}$ , the integral of Eq. (2) for a single facet reduces to

$$(\mathbf{a}_{\text{SRP}})_{\hat{L}=\hat{N}}^{\text{mirror}} = \frac{(\mathbf{a}_{\text{SRP}})_{\hat{L}=\hat{N}}^{\text{mirror}}}{1 + F_0} \left( 1 + \int_0^{2\pi} \int_0^{\pi/2} f_r \cos^2 \theta_r \sin \theta_r d\theta_r d\phi_r \right) \quad (\text{A1})$$

and Eq. (6) reduces to

$$(\mathbf{a}_{\text{SRP}})_{\hat{L}=\hat{N}}^{\text{mirror}} = \frac{(\mathbf{a}_{\text{SRP}})_{\hat{L}=\hat{N}}^{\text{mirror}}}{1 + F_0} [1 + (2\Delta_{s2} - \Delta_{s1})F_0] \quad (\text{A2})$$

where

$$(\mathbf{a}_{\text{SRP}})_{\hat{L}=\hat{N}}^{\text{mirror}} = -\frac{F_{\text{sun}} A_f}{m_{\text{SOC}}} (1 + F_0) \hat{N} \quad (\text{A3})$$

from Eq. (5). Note that  $\hat{V} \cdot \hat{N} = \cos \theta_r$  has been used in Eq. (A1). Combining Eq. (A1) and Eq. (A2) and setting  $\Delta = \Delta_{s1} = \Delta_{s2}$  yields

$$\Delta = \frac{1}{F_0} \int_0^{2\pi} \int_0^{\pi/2} f_r \cos^2 \theta_r \sin \theta_r d\theta_r d\phi_r \quad (\text{A4})$$

In the same limits, the Ashikhmin–Shirley BRDF in Eqs. (12) and (13) and Cook–Torrance BRDF in Eqs. (15–18) reduce to

$$f_r(\alpha) = \frac{F_0(n+1)}{8\pi} \cos^{n-1} \alpha \quad (\text{A5})$$

$$f_r(\alpha) = \begin{cases} \frac{F_0 e^{-[\tan \alpha/m]^2}}{4\pi m^2 \cos^4 \alpha \cos(2\alpha)} & \alpha < 30^\circ \\ \frac{F_0 e^{-[\tan \alpha/m]^2}}{2\pi m^2 \cos^4 \alpha} & \alpha > 30^\circ \end{cases} \quad (\text{A6})$$

In this geometry, there is a simple relation between the normal angle of the observer  $\theta_r$ , and the normal angle of the bisector between the illumination and observer  $\alpha$ , namely  $\alpha = \theta_r/2$ , and there is no azimuthal dependence. As a result, the integral of Eq. (A4) can be done analytically in both cases to compute  $\Delta$ . The resulting factors are given in Eqs. (26) and (27).

In the step 2 derivations of Sec. IV, with  $s = 1$  and  $n \rightarrow \infty$  (Ashikhmin–Shirley) or  $m \rightarrow 0$  (Cook–Torrance), the Ashikhmin–Shirley and Cook–Torrance BRDFs reduce to the same function, given by

$$f_r = \frac{F \delta(\hat{V} - \hat{R})}{\cos \theta_i} \quad (\text{A7})$$

which is nearly identical to the specular portion of the mirror-like term of Eq. (4) except that  $F_0$  is replaced by  $F$ . For the Ashikhmin–Shirley BRDF, this is Schlick’s approximation, which is given by Eq. (13), whereas for the Cook–Torrance BRDF, this is the Fresnel reflection from a perfectly smooth surface assuming the absorption coefficient is zero, which is given by Eq. (18). As with the simplified BRDF of Eq. (4), the integral of Eq. (2) can be done analytically in both cases and compared to Eq. (6) to compute  $\Delta$ . The resulting factors are given in Eqs. (28) and (29).

### Acknowledgements

This work is sponsored by a Small Business Innovative Research (SBIR) contract FA9453-11-C-0154 by the U.S. Air Force Research Laboratory at Kirtland Air Force Base, and contract FA8655-11-1-3043 by the European Office of Aerospace Research and Development, London, UK. The authors also wish to acknowledge useful discussions and technical contributions made by other members of the SBIR team: Daron Nishimoto, Keric Hill, Steve Lyke, Kris Hamada, and Channing Chow of Pacific Defense Solutions, LLC.

### References

- [1] Schildknecht, T., Musci, R., Flury, W., Kuusela, J., de Leon, J., and De Fatima Dominguez Palmero, L., “Properties of the High Area-to-Mass Ratio Space Debris Population in GEO,” *The Advanced Maui Optical and Space Surveillance Technologies Conference*, Wailea, Maui, HI, Sept. 2005, pp. 216–223.
- [2] Kelecy, T., Payne, T., Thurston, R., and Stansbery, G., “Solar Radiation Pressure Estimation and Analysis of a GEO Class of High Area-to-Mass Ratio Debris Objects,” *AAS Astrodynamics Specialist Conference*, Vol. 129, Mackinac Island, MI, Paper 07-391, Aug. 2007, pp. 2205–2221;
- [3] Kelecy, T., Baker, E., Seitzer, P., Payne, T., and Thurston, R., “Prediction and Tracking Analysis of a Class of High Area-to-Mass Ratio Debris Objects in Geosynchronous Orbit,” *The Advanced Maui Optical and Space Surveillance Technologies Conference*, Wailea, Maui, HI, Sept. 2008, p. 33.
- [4] Kelecy, T., and Jah, M., “Analysis of Orbit Prediction Sensitivity to Thermal Emissions Acceleration Modeling for High Area-to-Mass Ratio (HAMR) Objects,” *The Advanced Maui Optical and Space Surveillance Technologies Conference*, Wailea, Maui, HI, Sept. 2009, p. 17.
- [5] Kelecy, T., and Jah, M., “Analysis of High Area-to-Mass Ratio (HAMR) GEO Space Object Orbit Determination and Prediction Performance: Initial Strategies to Recover and Predict HAMR GEO Trajectories with No A Priori Information,” *Acta Astronautica*, Vol. 69, Nos. 7–8, 2011, pp. 551–558.  
doi:10.1016/j.actaastro.2011.04.019
- [6] Kelecy, T., Jah, M., and DeMars, K., “Application of a Multiple Hypothesis Filter to Near GEO High Area-to-Mass Ratio Space Objects State Estimation,” *Acta Astronautica*, Vol. 81, No. 2, 2012, pp. 435–444.  
doi:10.1016/j.actaastro.2012.08.006
- [7] Linares, R., Crassidis, J. L., Jah, M. K., and Kim, H., “Astrometric and Photometric Data Fusion for Resident Space Object Orbit, Attitude, and Shape Determination Via Multiple-Model Adaptive Estimation,” *AIAA Guidance, Navigation, and Control Conference*, Curran Associates Incorporated, Toronto, Ontario, Canada, Paper 2010-8341, Aug. 2010.
- [8] Ziebart, M., “Generalized Analytical Solar Radiation Pressure Modeling Algorithm for Spacecraft of Complex Shape,” *Journal of Spacecraft and Rockets*, Vol. 41, No. 5, 2004, pp. 840–848.  
doi:10.2514/1.13097
- [9] Ashikhmin, M., and Shirley, P., “An Anisotropic Phong BRDF Model,” *Journal of Graphics Tools*, Vol. 5, No. 2, 2000, pp. 25–32.  
doi:10.1080/10867651.2000.10487522
- [10] Cook, R. L., and Torrance, K. E., “A Reflectance Model for Computer Graphics,” *ACM Transactions on Graphics*, Vol. 1, No. 1, Jan. 1982, pp. 7–24.  
doi:10.1145/357290.357293
- [11] Schlick, C., “An Inexpensive BRDF Model for Physically-Based Rendering,” *Computer Graphics Forum*, Vol. 13, No. 3, 1994, pp. 233–246.  
doi:10.1111/cgf.1994.13.issue-3
- [12] Gautschi, W., and Cahill, W. F., “Exponential Integral and Related Functions,” *Handbook of Mathematical Functions With Formulas, Graphs, and Mathematical Tables*, edited by Abramowitz, M., and Stegun, I. A., National Bureau of Standards Applied Mathematics Series, Washington, DC, 1964, p. 272.
- [13] Knocke, P. C., Ries, J. C., and Tapley, B. D., “Earth Radiation Pressure Effects on Satellites,” *Proceedings of the AIAA/AAS Astrodynamics Conference*, Minneapolis, MN, Paper 88-4292-CP, Aug. 1988, pp. 577–587.
- [14] McCarthy, J. J., and Martin, T. V., “A Computer Efficient Model of Earth Albedo Satellite Effects,” NASA Goddard Space Flight Center, Planetary Sciences Dept., Rept. 012-77, 1977.
- [15] Rakhamanov, E. A., Saff, E. B., and Zhou, Y. M., “Minimal Discrete Energy on the Sphere,” *Mathematical Research Letters*, Vol. 1, No. 6, 1994, pp. 647–662.
- [16] Saff, E. B., and Kuijlaars, A. B. J., “Distributing Many Points on a Sphere,” *The Mathematical Intelligencer*, Vol. 19, No. 1, 1997, pp. 5–11.  
doi:10.1007/BF03024331
- [17] Marshall, J. A., and Luthke, S. B., “Modeling Radiation Forces Acting on Topex/Poseidon for Precision Orbit Determination,” *Journal of Spacecraft and Rockets*, Vol. 31, No. 1, 1994, pp. 99–105.  
doi:10.2514/3.26408
- [18] Vallado, D. A., *Fundamentals of Astrodynamics and Applications*, 3rd ed., McGraw-Hill, New York, 2007, pp. 574–578.
- [19] Shuster, M. D., “A Survey of Attitude Representations,” *Journal of the Astronautical Sciences*, Vol. 41, No. 4, Oct.–Dec. 1993, pp. 439–517.